

New *ab initio* approach for high pressure systems with application to a new high-pressure phase for boron: perturbative momentum-space potentials.

D.E. Segall^{†1} and T.A. Arias²

¹*Department of Physics, Massachusetts Institute of Technology, Cambridge MA 02139*

²*Laboratory of Atomic and Solid State Physics, Cornell University, Ithaca, NY 14853*

Through the use of perturbation theory, in this work we develop a method which allows for a substantial reduction in the size of the plane-wave basis used in density-functional calculations. This method may be used for both pseudopotentials and all-electron calculations and is particularly beneficial in the latter case. In all cases, the approach has the advantage of allowing accurate predictions of transferability errors for any environment. Finally, this method can be easily implemented into conjugate gradient techniques and it is therefore computationally efficient. In this work, we apply this method to study high pressure phases of boron. We find that boron undergoes a phase transition from the icosahedral family to the α_{ga} -B structure, both of which are semiconducting. The α_{ga} -B structure has lower energy than traditional mono-atomic structures, which supports the assertion that the metallic, and hence superconducting phase, for boron is much more complicated than a simple mono-atomic crystal. Moreover, we argue that the β_{ga} -B structure could be a candidate for the superconducting phase of boron.

I INTRODUCTION

Experimental techniques are now able to probe condensed matter systems at higher and higher pressures through the use of diamond-anvil cells or dynamical shock methods.^{1,2} At these newly attainable pressures, structural and electronic phase transitions can occur, opening the door to exploration for new physical phenomena.

Such systems offer an exciting avenue for first principle calculations, as their predictions can not only follow but also sometimes lead results from new experimental techniques.²⁻⁹ When applying traditional first principle calculations to such systems, care must be taken, as most basis sets take advantage of the distinction between the core regions and valence regions which is prominent at ambient conditions. However, when studying systems over a wide range of pressures, this distinction vanishes, and both regions need to be treated on an equal footing. The following section discusses some problems that can occur when applying some of the most popular basis sets to high pressure systems.

To overcome the above potential pitfalls and to allow for accurate description of both the core and valence regions while keeping the mathematical stability and systematic convergence of the plane-wave basis, we have developed a method based on perturbation theory. This method can be used for direct all-electron calculations, dramatically reduces the size of the plane-wave basis while properly accounting for all higher momen-

tum states, accounts accurately for the core electrons and their interaction with the valence region, and automatically generates pseudopotentials which change with the environment thereby enhancing transferability. Moreover, the effect of pseudizing in the crystal can be quantified; hence, accurate predictions for transferability can be made in *any* environment. Finally, the method can be implemented into current state of the art minimization techniques, such as the conjugate gradient method, and is therefore computationally efficient.

As an application, we study high pressure phases of boron. Boron crystallizes into many complex structures, which are governed by the regular icosahedron.^{10,11} Boron is semiconducting at ambient conditions, turns metallic under pressure (≈ 170 GPa²) and superconducting above 160 GPa.² Theoretically, Mailhot and coworkers⁹ were the first to apply density-functional techniques to the study of the phases of Boron at high pressures. To date, however, such studies have been limited to a modest selection of phases and were based on traditional techniques which artificially separate the physics in the core and valence regions. In this work, we apply our new, unbiased technique to a wider range of phases and find a new phase, the α_{ga} -B structure, to be lower in energy at high pressure than any phase reported previously and to have important potential implications for the observed semiconductor-metallic phase transition associated with the superconductivity.

We proceed as follows: Section II describes the various methods that can be used to study systems under

[†]Current Address: Department of Mechanical Engineering, California Institute of Technology, Pasadena, California 01125.

high pressure, specifically, the pros and cons of each method. Then our method is developed and tested in Sections III and IV. Finally, we will apply our approach to study the high pressure phases of boron in Section V.

II METHODS

Within current state of the art electronic structure calculations, various approaches can be taken, mainly differentiated by the choice in basis set. Each set has its own benefits and disadvantages. Some of the most common basis sets are the plane-waves,¹² Gaussian,¹³ linearized methods,^{14,15} and wavelets.¹⁶ We will now go over the various basis sets and focus on problems that may occur when each is applied to high pressure systems.

The Gaussian basis set expands the wave functions in terms of linear combinations of Gaussians designed to represent the atomic orbitals well. Such a basis set has the advantageous property of expanding the wave functions in a small number of computationally efficient basis functions. There are, however, some drawbacks. Notably, such a basis set cannot be improved systematically. This does not tend to be a practical problem for normal systems; however, such a problem can manifest itself for a system studied at various volumes, as the basis set will span a different percentage of real space for systems whose volume differ appreciably. Because it is unclear of how to convergence such a basis set systematically, it is unknown whether standard Gaussian basis sets will perform well at high-pressures, particularly because such bases are biased toward orbitals constructed at ambient conditions. It is thus unclear if such a bias can hamper calculations at high pressures, where unknown phenomena may occur.

Linearized methods generally fall under one of two methods: the Linear Muffin Tin Orbital (LMTO)¹⁵ method or the Linearized Augmented Plane-Wave (LAPW)¹⁴ method. Of these two, the LAPW is more accurate and we will therefore concentrate on this approach. When studying systems under high pressure, the most notable problem that can occur with the LAPW method is the treatment of the core electrons. At high pressures, certain core electrons need to be promoted and treated as valence electrons, and care must be taken with this method when promoting such electrons. Two widely used approaches to promote such electrons are the multiple window approach¹⁴ and the localized orbital approach.¹⁴ Both of these approaches could be particularly problematic for high pressure systems, particularly for first row elements. The multiple window method is not guaranteed to give a good solution,¹⁴ as different basis sets are used to expand the core and valence electrons. In the localized orbital approach, this problem is resolved by using one energy window. However, problems may exist, as there are very large energy separations between the valence bands and the core bands, particularly for first

row elements.

The plane-wave approach, when used with the pure Coulomb potential, has the advantageous property that convergence of the energy can be systematically improved in a stable and controllable framework. Moreover, such a basis is unbiased and can therefore represent core and valence regions on an equal footing. However, such an approach has only been used for the simplest systems, such as hydrogen¹⁷⁻¹⁹ and lithium¹⁹ as it requires a huge number of plane-waves to properly account for the singular Coulomb potential and the exclusion principle. Therefore such an approach is not practical beyond the simplest systems.

The pseudopotential approach had been developed to circumvent the above difficulties with plane waves bases.²⁰⁻²² However, pseudopotentials are poorly suited for studying high pressure systems because, although some key properties are known,^{20,23,24} the transferability of pseudopotentials is not systematically understood, particularly when the pseudized regions occupy a large percentage of the available volume as they do at high densities. More fundamentally, apart from nonlinear core corrections in the exchange-correlation potential,²⁵ pseudopotentials completely ignore the core region, which have been shown to play a vital role for high pressure systems.^{3,4}

One of the most successful techniques, which keeps the benefits of the pseudopotential approach and can allow for core electrons and can recover details of the true wave function in the core region, is the Projected Augmented Wave (PAW)²⁶ method. This method has been used to study Lithium and Sodium^{3,4} under high pressure. Such a method is quite elegant; however, it must be constructed from a referenced atomic state. Moreover, the construction of such a potential still requires a real space cutoff. In order to effectively study high pressure systems, such a cutoff should be made quite small, so that the pseudized regions do not overlap. The approach then loses many of its computational benefits.

The final type of basis set of which we are aware in the study of solid state systems are wavelet bases.¹⁶ Such bases have the attractive property of using multi-resolution analysis to provide the necessary resolution in each region of space in a systematic and mathematically stable manner and thereby efficiently handle valence and core electrons exactly. However, such a basis set has just come to the fore and has not yet been adopted by many groups.

We now describe a technique which has the advantage of using a plane-wave basis without pseudopotentials. This method has the added benefit of greatly reducing the size of the plane-wave basis set by generating the important high momentum states through perturbation theory. Below, we show that a properly constructed perturbation expansion can be quite accurate in this context. Finally, we show that this method can easily be implemented in current conjugate gradient techniques and therefore can be used with highly optimized minimization

techniques.

III PERTURBATIVE DERIVATION

In the next two sections, the method will be derived. To gain insight into this method, it will first be derived for the simple case of directly diagonalizing the single-particle Hamiltonian. Then, connections will be made to previous approaches.²⁷ In Section IV, the procedure will be implemented into the conjugate gradient framework, so that optimized calculations can be performed. Technical details will be discussed in Section IV C. For simplicity in the formal developments below, we sample the Brillouin zone at the Gamma point. Adding in k -point dependence is straightforward.

A Derivation for fixed potentials

Standard electronic structure calculations seek for the minimum of an energy functional $E[\{C\}]$ as a function of a set of basis function coefficients $\{C\}$ subject to an orthonormality constraint. The variational derivative of this energy functional and constraint then lead to the standard eigenvalue problem

$$HC = \epsilon C, \quad (1)$$

where H is the single-particle Hamiltonian (fixed and not updated self-consistently for the discussion in this section), C is an eigenvector and ϵ is the corresponding eigenvalue. Note that we here assume that the basis set is orthonormal as our objective here is to work with plane waves.

Separating the coefficients into two groups, those describing behavior in the low spatial frequency space P as C^P and those describing behavior in the high spatial frequency space Q as C^Q , also separates the couplings which H describes into four groups, couplings from low-frequency to low-frequency H^{PP} , from low- to high-frequency H^{QP} , from high to low H^{PQ} and from high to high H^{QQ} . The above equation then decomposes simply into

$$H^{PP}C^P + H^{PQ}C^Q = \epsilon C^P \quad (2)$$

$$H^{QP}C^P + H^{QQ}C^Q = \epsilon C^Q. \quad (3)$$

Solving for the Q -space components of the eigenfunction in terms of the P -space components leads to

$$C^Q = -\frac{1}{H^{QQ} - \epsilon} H^{QP} C^P, \quad (4)$$

where the fraction means the inverse of an operator.

A standard technique²⁷⁻²⁹ is to substitute Equation (4) into Equation (2) in order to generate an effective eigenvalue equation for the P -space,

$$(H^{PP} + H^{PQ} \frac{1}{\epsilon - H^{QQ}} H^{QP}) C^P = \epsilon C^P. \quad (5)$$

This equation reduces the problem to the P -space only. If standard diagonalization techniques are used, this reduces the time to diagonalize the Hamiltonian by a factor of $(\frac{N^P}{N^P + N^Q})^3$, where N^α is the number of basis functions in the α -space. However, it is well known that such a decomposition does not necessarily simplify the problem at hand, particularly because inversion of a matrix is computationally intensive and care must be taken in order to achieve self-consistency in the eigenvalue. We now describe an efficient way to go beyond the standard approach to address each of these issues in turn.

In a plane-wave basis, the inversion of $\epsilon - H^{QQ}$ can be approximated accurately and simply in a way which will save considerable computational effort, especially when used in conjunction with conjugate gradient techniques. Specifically, because the Q -space contains the high momentum plane-wave states, the kinetic energy dominates H^{QQ} , which we may then approximate to be the kinetic energy operator H_o^{QQ} , whose α, β component is

$$H_{o,\alpha\beta}^{QQ} = \frac{1}{2} \vec{Q}_\alpha^2 \delta_{\alpha,\beta}. \quad (6)$$

Here $\delta_{\alpha,\beta}$ is the Kronecker delta and \vec{Q} is a reciprocal lattice vector, and atomic units have been assumed.

In principle, the eigenvalues appearing in the left side of Equation (5) must be calculated self-consistently, but this leads to difficulties. Each eigenstate sought then sees a different Hamiltonian and orthonormality is lost. Alternately, in practice one employs on the left-hand side a constant, approximate ϵ which one hopes to be appropriate for all desired eigenvalues. For us, neither approach is satisfactory. To circumvent these difficulties, we linearize C^Q in terms of the eigenvalue

$$C^Q = -\frac{1}{H_o^{QQ}} (1 + \frac{\epsilon}{H_o^{QQ}}) H^{QP} C^P + \mathcal{O}(\frac{\epsilon}{H_o^{QQ}})^2. \quad (7)$$

Note that in a plane-wave basis such an expansion will converge quickly, as the cutoff in the P -space is, in general, much larger than the eigenvalues of interest.

Substituting Equation (7), to linear order in ϵ , into Equation (2), gives an effective generalized eigenvalue equation,

$$(H^{PP} + H^{eff}) C^P = \epsilon O C^P. \quad (8)$$

Here

$$H^{eff} = -H^{PQ} \frac{1}{H_o^{QQ}} H^{QP} \quad (9)$$

is the effective single-particle Hamiltonian and

$$O = 1 + H^{PQ} \frac{1}{H_o^{QQ}} \frac{1}{H_o^{QQ}} H^{QP} \quad (10)$$

is a positive-definite overlap matrix. This equation will generate errors of order $(\epsilon/E_c^P)^2$ in the eigenvalue, where E_c^P is the cutoff energy for the P -space. We below, we show that this truncation error proves to be a good measure of the error in the energy per atom. Thus, our method provides for accurate *a priori* predictions for transferability errors.

In addition to computing the eigenvalue spectrum, we often require access to the eigenstates, particularly for density functional theory calculations which require self-consistent solution of the electronic states within a potential dependent upon those states. Calculation of the self-consistent potential requires not only the P -space components C^P from (8) but also the Q -space components. The most direct choice for generating the C^Q is to use Equation (7); however, we wish to eventually apply this technique to the conjugate gradient method and defining C^Q as in Equation (7), no longer preserves orthonormality for the full eigenvector set $\{C\}$ and post-reorthonormalization can make the conjugate gradient procedure unstable.

To avoid these difficulties, we note that the solutions to the generalized eigenvalue problem (8) automatically satisfy

$$\begin{aligned}\delta_{ij} &= C_i^{P\dagger} \mathcal{O} C_j^P \\ &= C_i^{P\dagger} \left(1 + H^{PQ} \frac{1}{H_o^{QQ}} \frac{1}{H_o^{QQ}} H^{QP} \right) C_j^P\end{aligned}$$

where the subscripts indicate the coefficients for individual states i and j and we have substituted the definition (10). Regrouping terms, we find that identically

$$\delta_{ij} = C_i^{P\dagger} C_j^P + \left(-\frac{1}{H_o^{QQ}} H^{PQ} C_j^P \right)^\dagger \left(-\frac{1}{H_o^{QQ}} H^{PQ} C_j^P \right),$$

so that the set of complete states $\{C\}$ will be exactly orthonormal provided we make the identification,

$$C^Q \equiv -\frac{1}{H_o^{QQ}} H^{QP} C^P, \quad (11)$$

which is nothing other than (7) truncated at zeroth order. We thus conclude that to avoid issues of orthonormality to allow simple implementation of conjugate gradient techniques, one *must* construct C^Q at this order. Accordingly, we employ (11) as the construction for C^Q throughout the remainder of this work.

B Connections with Löwdin Perturbation Theory

To carry out full density-functional calculations based upon the results from the previous section, one in principle first would solve (8) using direct diagonalization techniques to find C^P and then construct C^Q from (11). Next, from the wave functions, one would update the

charge density, Hartree and exchange-correlation potentials, recompute H^{PP} , H^{eff} and \mathcal{O} . Finally, one would iterate this procedure to self-consistency. As this approach is quite similar to the Löwdin perturbation theory²⁷ which was used in the mid 1980's by a number of groups^{30,31} with regard to electronic structure calculations, this section briefly reviews the Löwdin approach as described in Reference³⁰ and discuss the major differences between that approach and ours. The following section, Section , shows how conjugate gradient techniques may be applied directly to our approach but not to Löwdin perturbation theory.

Löwdin perturbation theory also decomposes behavior into high and low momentum plane-wave states. This approach also solves an eigenvalue problem $U^{PP} C^P = \epsilon C^P$ for a renormalized Hamiltonian U^{PP} similar to that of Equation (5),

$$U^{PP} = H^{PP} + H^{PQ} \frac{1}{\epsilon - H_o^{QQ}} H^{QP}, \quad (12)$$

Self-consistency is reached by calculating the charge density either with C^P alone, or with both C^P and C^Q , with as

$$C^Q = \frac{1}{\epsilon - H_o^{QQ}} U^{QP} C^P. \quad (13)$$

Here U^{QP} is similar to U^{PP} , except that the first index is in the Q -space. For the reasons discussed above in Section III A, if C^Q is employed, then the wave functions must be re-orthonormalized.

In practice,³⁰ the value employed for ϵ in Equation (12) depends upon the physics under exploration. Thus, prior to the calculation, the shape of the band structure should be approximately known and should have a relatively narrow band-width, requiring great care for the study of systems under unusual physics conditions such as extremely high pressures. Moreover, the approximation of ϵ by $\tilde{\epsilon}$ is always a first order error in the solution to the eigenvalue. This can simply be seen by Taylor expanding Equations (12) and (13) in a similar fashion as Equations (7) and (8). If $\tilde{\epsilon}$ is close to ϵ , then this error is small as is the next order. However, if there is a large discrepancy between ϵ and $\tilde{\epsilon}$, then these errors are *manifestly* first order. This is particularly troublesome for calculations including core electrons where the core states energies have large separations from the valence states. We thus expect Löwdin perturbation to be useful primarily only within a pseudopotential framework. In our approach, by contrast, *all* band energies are treating on an equal footing to second order. This is because Equation (8) includes all terms through first order by shifting some terms to the right-hand side to form the generalized eigenvalue problem.

The great advantage of Löwdin perturbation theory for its time is that it reduces the time for standard diagonalization from $(N^P + N^Q)^3$ to $(N^P)^3$. However, in the mid 1980's standard diagonalization techniques were dropped in lieu of much more efficient Car-Parrinello^{32,33} and

conjugate gradient^{33–35} techniques, which, being based on minimization, require the the eigenvalue equations to represent the variational derivative of some energy functional. It is not clear that the Hamiltonian used within Löwdin perturbation theory is a good approximation to the variational derivative of an energy functional. What particularly complicates this is the dependence of the Hamiltonian on the eigenvalue and that the unfolding of the wave vector into the Q -space does not preserve orthonormality. Therefore, it is unclear how one would employ Löwdin perturbation theory in conjunction with such optimized minimization techniques. The next section demonstrates that, in contrast, our approach represents a very good approximation to the variational derivative of an energy functional and, because it preserves orthonormality, can be used directly with optimized minimization techniques.

IV APPLICATIONS TO CONJUGATE GRADIENT TECHNIQUES

We first discuss applicability to a traditional conjugate gradient techniques in Section IV A and generalize to the analytic continued approach^{35,36} in Section IV B. Section IV C gives details of our computational implementation and Section IV D provides specific computational studies of the various approximations and the convergence of the approach.

A Application to Traditional Conjugate Gradient Techniques

Again, we seek the minimum of an energy functional of the form $E[\{C\}]$ as a function of a set of wave function coefficients $\{C\}$. To formulate the separation into low- and high- spatial frequency components as a variational principle associated with an energy functional, we express the energy functional directly in terms of the $\{C^P\}$ and $\{C^Q\}$ before taking any variations, $E[\{C^P\}, \{C^Q\}]$. We now seek the minimum of this functional subject to the orthonormalization condition

$$C_i^{P\dagger} \mathcal{O} C_j^P = \delta_{ij}. \quad (14)$$

Here \mathcal{O} is an overlap matrix, which should give the correct overlap matrix at the minimum of the energy functional. Section IV C will describe the overlap matrix that we use in our calculations. Finally, the $\{C^Q\}$ are left *unconstrained*.

The sets $\{C^P\}$ and $\{C^Q\}$ are treated as independent variables. However, at each $\{C^P\}$ point, the functional is directly minimized with respect to the set $\{C^Q\}$. The gradients are

$$\frac{\partial E}{\partial C_i^{P\dagger}} = H^{PP} C_i^P + H^{PQ} C_i^Q - \epsilon \mathcal{O} C_i^P \quad (15)$$

and

$$\frac{\partial E}{\partial C_i^{Q\dagger}} = 0 = H^{QP} C_i^P + H^{QQ} C_i^Q, \quad (16)$$

where the second term is set to zero, emphasizing that the energy functional is minimized with respect to $\{C^Q\}$ at each point $\{C^P\}$.

The flowchart in Figure 1 describes the minimization procedure within the traditional conjugate gradient framework. Given a point at $\{C^P\}$ and $\{C^Q\}$, calculate the energy. Next, calculate the gradient for the set $\{C^P\}$, Equation (15) or (18), and hold the set $\{C^Q\}$ fixed. Minimize the energy functional for the set $\{C^P\}$ only, along the conjugate direction $\{X^P\}$. After the functional is minimized along this particular direction, the functional is then minimized with respect to $\{C^Q\}$, Equation (16), by setting

$$C^Q = -\frac{1}{H_o^{QQ}} H^{QP} C^P. \quad (17)$$

Finally, this process iterates until the energy functional reaches its minimum.

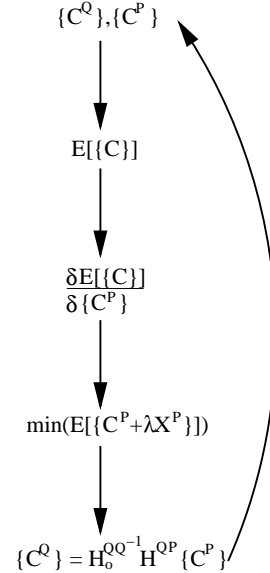


FIG. 1: Flow chart for application to traditional conjugate gradient techniques.

In calculating C^Q , we have again approximated H^{QQ} by H_o^{QQ} , and therefore do not exactly minimize C^Q . Although the form for C^Q is not that which exactly minimizes our functional, we have found the approximation to be sufficiently close that the conjugate gradient technique is quite stable and efficient. Using such a form for C^Q , the gradient for C^P indeed becomes

$$\frac{\partial E}{\partial C_i^{P\dagger}} = H^{PP} C_i^P + H^{eff} C_i^P - \epsilon \mathcal{O} C_i^P, \quad (18)$$

where H^{eff} is as defined in Equation (9). Thus, we find that, unlike the Löwdin perturbation theory approach, the prescription in Section III A represents a set of equations to represent to a very good approximation a variational principle and therefore to be amenable to solution with conjugate gradient methods.

To underscore the effectiveness of conjugate-gradient methods for use within our framework, Figures 2 and 3 show the iterative convergence of the total energy within the local density approximation (LDA)³⁷ to density-functional theory for cubic hydrogen and an eight atom cell of fcc carbon, respectively. The calculations use the preconditioner of Teter, Payne and Allen,³⁴ cutoffs of $E_c^P = 8$ H and $E_c^Q = 16$ H for hydrogen and $E_c^P = 30$ H and $E_c^Q = 60$ H for carbon, and the overlap operator \mathcal{O} from Section IV C. The hydrogen calculation uses the pure Coulomb potential and an $8 \times 8 \times 8$ Monkhorst-Pack³⁹ sampling grid, and the carbon calculation uses the Goedecker, Teter and Hunter pseudopotential³⁸ with simple Γ -point sampling. Finally, the cubic lattice constants were 2.753 bohr and 6.746 bohr for sc hydrogen and fcc carbon, respectively.

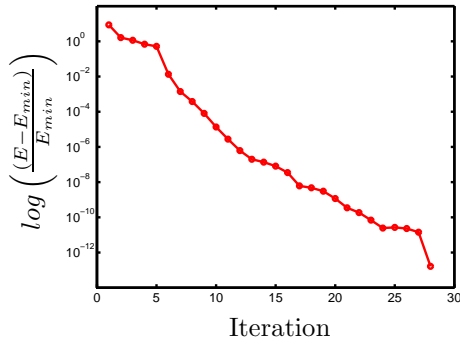


FIG. 2: Energy error versus iteration number for the new method, within the conjugate gradient framework for simple cubic hydrogen when using the Coulomb potential.

It can be seen that the conjugate gradient technique is stable and that fluctuations occur only in the final stages when the error is $\Delta E/E_{min} \approx 10^{-10}$, well within acceptable convergence. These fluctuations are associated with the fact that $H_{\mathcal{O}}^{QQ}$ is used instead of H^{QQ} . In general, we have found that the stability of the conjugate gradient does not depend on the approximation for C^Q , but mainly depends on how and when we update C^Q . Table I compares the error in the energy per atom with the new approach, with cutoffs stated above, to that with the traditional approach, with cutoff $E_c^{trad} = E_c^P$. The fully converged results are considered to be that of the traditional approach with energy cutoff $E_c^{conv} = E_c^Q$. The results for the new procedure show a vast improvement.

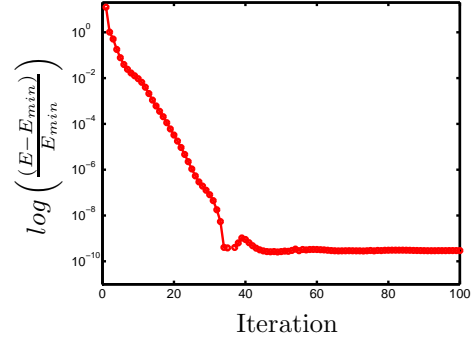


FIG. 3: Energy error versus iteration number for the new method, within the conjugate gradient framework for fcc carbon when using a nonlocal pseudopotential.

As noted above, one of the advantages of our approach is that it allows for an *a priori* estimate of the transferability errors. We define this *transferability prediction* as

$$\Delta E_{new}^{predict} = \sum_{states} \epsilon_{states} (\epsilon_{states}/E_c^P)^2, \quad (19)$$

where the sum is over occupied states. For the specific cases of the present two calculations, our prediction gives $\Delta E_{new}^{predict} \approx 0.5(0.5/8)^2 \approx 2mH$ for hydrogen and $\Delta E_{new}^{predict} \approx 2 \times 0.5(0.5/30)^2 \approx 0.2mH$ for carbon, where for simplicity we consider only the 2 s-states. These predictions also appear in Table I. The predicted values are very similar to ΔE_{new} , demonstrating that this prediction, which may be applied in *any* environment, gives sensible estimates of the errors.

	$\Delta E_{trad}(E_c = E_c^P)$	ΔE_{new}	$\Delta E_{new}^{predicted}$
Hydrogen (sc)	9mH	1mH	2mH
Carbon (fcc)	16mH	0.3mH	0.2mH

TABLE I: The error in calculating the energy per atom for simple cubic hydrogen and fcc carbon. The first column shows the error in energy when using the traditional approach. The next column shows the error in energy when using the new approach. The final column shows the transferability prediction of the new approach, Equation (19).

Sections IV D and V show that in practice the present method is particularly beneficial for all-electron calculations of first row elements, where the reduction in the cutoffs is much more dramatic than the cases presented here.

B Application in the Analytic Continued Approach

Our procedure can be easily incorporated into the analytic continued conjugate gradient approach.³⁵ In such

an approach, constrained variables, $\{C\}$, are not minimized, but unconstrained variables $\{Y\}$ are minimized. This approach allows for much better convergence, as all directions are allowed in the search space when minimizing the energy functional.³⁵

In the analytic continued approach, the sets $\{C\}$ and $\{Y\}$ are related by

$$\mathbf{C} = \mathbf{Y}u^{-\frac{1}{2}}V^\dagger, \quad (20)$$

where bold faced quantities refer to the expansion coefficients for all states gathered into matrices, each of whose columns represents a particular state. Here, V is a unitary transformation which allows for subspace rotations^{35,36} and u is the expectation value of \mathbf{Y} with respect to the overlap matrix \mathcal{O} ,

$$u = \mathbf{Y}^\dagger \mathcal{O} \mathbf{Y}. \quad (21)$$

Note that Equation (20) is constructed so that the \mathbf{C} automatically satisfy the orthogonality constraint (14), as direct substitution verifies. This approach allows the total energy to be found by minimizing the energy $E[\mathbf{Y}]$ directly using standard, unconstrained conjugate-gradient techniques.

In our case, the gradient becomes

$$\frac{\partial E}{\partial \mathbf{Y}^{P\dagger}} = (1 - \mathcal{O}\mathbf{C}^P\mathbf{C}^{P\dagger})(H^{PP} + H^{eff})\mathbf{C}^P F V U^{\frac{1}{2}} + \mathcal{O}\mathbf{C}^P V Q(V^\dagger[\tilde{H}, F]V), \quad (22)$$

where H^{eff} is as defined in Equation (9), F is a diagonal “filling” matrix composed of the state occupancies, \mathcal{O} is the overlap matrix, defined similarly to Equation (10), and $Q()$ is the Q -operator,^{35,36} defined by

$$(W^\dagger Q(A)W)_{nm} \equiv \frac{(W^\dagger A W)_{nm}}{\sqrt{\mu_n} + \sqrt{\mu_m}},$$

where W is the unitary, column order, eigenvector matrix for u and μ are the corresponding eigenvalues. In Equation (22), the Q -operator operates on the matrix $V^\dagger[\tilde{H}, F]V$, where $[\tilde{H}, F]$ is the commutator between the filling matrix F and the subspace Hamiltonian matrix,

$$\tilde{H} = \mathbf{C}^{P\dagger}(H^{PP} + H^{eff})\mathbf{C}^P.$$

Finally, the solution for \mathbf{C}^Q becomes

$$\mathbf{C}^Q = -\frac{1}{H_o^{QQ}}H^{QP}\mathbf{C}^P. \quad (23)$$

We note that H^{eff} in Equation (22) acts as a pseudopotential generated directly from the crystal environment and not from a referenced atomic calculation which one must hope to be transferable. The overlap matrix \mathcal{O} acts to preserve the correct orthonormalization for the P -space wave function. This overlap matrix is similar to those found in the Ultra-Soft Pseudopotentials (USSP)⁴⁰

and Projected Augmented Wave²⁶ methods. In those methods, the softening procedure is generated in a real space formalism, from a specific reference state, and depends on the choice of a cutoff in real space cutoff. In this work, the softening is done in a momentum space formalism without artificial core radii, making the procedure ideal for high-pressure studies where the loss of distinction between core and valence regions is precisely the physics of interest. As a final advantage of the present approach, Equation (19) gives a direct measure of transferability errors.

C Computational details

We will now describe briefly efficient calculation of specific terms in our procedure. The text focuses on all-electron calculations as these are of interest in the present work. The appendix discusses details for the use of this approach with hard but transferable Kleinman-Bylander pseudopotentials.

1 Form for overlap matrix

The overlap matrix has the form

$$\mathcal{O} = 1 + \left(H_{h,xc}^{PQ} + H_{ion}^{PQ} \right) \frac{1}{H_o^{QQ}} \frac{1}{H_o^{QQ}} \left(H_{h,xc}^{QP} + H_{ion}^{QP} \right), \quad (24)$$

where $\frac{1}{H_o^{QQ}}$ is the inverse of the kinetic energy, H_{ion} is the contribution from the local ionic potential and $H_{h,xc}$ is the contribution from the Hartree and exchange-correlation potentials, which depends on the density. There are a number of viable options for implementing \mathcal{O} . We have explored both the option of fixing $H_{h,xc}$, and thus \mathcal{O} to some value and the option of updating it self-consistently.

The benefit of holding the overlap matrix fixed is that

$$\frac{\partial \mathcal{O}}{\partial \mathbf{C}^{P\dagger}} = 0, \quad (25)$$

so that Equation (15) is the exact variational derivative of the energy functional. The appendix further shows that such a fixed operator makes efficient implementation of Kleinman-Bylander pseudopotentials possible. A clear choice for a fixed overlap matrix is to hold $H_{h,xc}$ in Equation (24) to that of the “free-atom” crystal, a crystal whose charge density is just the superposition of the charge densities from isolated atoms. In such a case, the overlap matrix becomes

$$\mathcal{O} = 1 + H^{cr-at,PQ} \frac{1}{H_o^{QQ}} \frac{1}{H_o^{QQ}} H^{cr-at,QP}, \quad (26)$$

where $H^{cr-at,PQ} = H_{h,xc}^{cr-at,PQ} + H_{ion}^{PQ}$ and $H_{h,xc}^{cr-at,PQ}$ is Hartree and exchange-correlation potential for the “free-atom” crystal. One possible cause for concern when using a fixed overlap matrix is that the orthonormalization is no longer exact (so that, for instance, the electronic charge will not be precisely conserved) because H^{QP} in Equation (23) will differ from its free-atom crystal value. However, we have found this to never affect the convergence of the calculations and to yield quite accurate results, as Figures 2 and 3 and Table I show.

Alternately, exact orthonormalization can be preserved when using a fixed overlap operator if one chooses to re-define \mathbf{C}^Q as

$$\mathbf{C}^Q = -\frac{1}{H_o^{QQ}} H^{cr-at,QP} \mathbf{C}^P. \quad (27)$$

While this preserves orthonormality among the states, it does give a slightly different approximation to \mathbf{C}^Q , which causes a slight change in the H^{eff} which should be used in (8). We find, however, that ignoring this discrepancy makes no practical difference in the final results. With this alternate approach, the convergence is quite similar to those of Figures 2 and 3, and the energy per atom is within 1μ H, as compared to using Equation (23) for \mathbf{C}^Q . Another benefit of using the form Equation (27) comes when using non-local pseudopotentials, as this form is computationally more efficient. (See the appendix for details.)

Finally, the H^{eff} which should be used with the construction in Equation (27) is

$$H^{eff} = -H^{PQ} \frac{1}{H_o^{QQ}} H^{cr-at,QP}. \quad (28)$$

Maintaining this consistency comes at the cost of introducing a slightly non-Hermitian Hamiltonian. Despite this, we again have not experienced any practical problems working with this form.

The second option for implementing the overlap matrix is to use the Hartree and exchange correlation potentials self-consistently. When doing so, the gradient of the total energy involves terms including the derivative of the overlap matrix. Unfortunately, we have yet to find a method for calculating these contributions to the gradient which does not require multiplication by matrices of size $N^P \times N^P$, a completely impractical feat for all but the most trivial of systems.

We have found somewhat to our surprise, however, that updating the overlap matrix self-consistently while completely ignoring these contributions to the gradient that, despite that with this approximated gradient, the gradient technique remains stable and maintains its good convergence, as Figures 4 and 5 show. In these calculations, $H_{h,xc}^{cr-at}$ was used only at the first iteration to initialize the calculation. After that, the overlap was updated self-consistently and the gradient was always calculated ignoring the aforementioned contributions from the changes in \mathcal{O} . The discontinuity in Figure 4 is a

result of the fact that the error in the variational derivative is larger than before, as H_o^{QQ} and H^{cr-at} were only minor discrepancies. Perhaps a more stable approach would be to use $H_{h,xc}^{cr-at}$ for a number of iterations and then restart the conjugate gradient techniques using the self-consistent overlap matrix. In any event, we find the final energy per atom again to be within 1μ H of all of the approaches above.

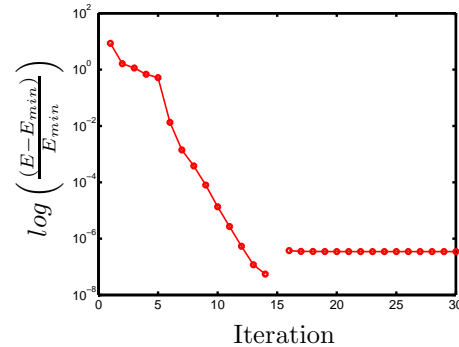


FIG. 4: Energy convergence versus iteration for simple cubic hydrogen when the overlap matrix is updated self-consistently, but its variational derivative is not taken into account.

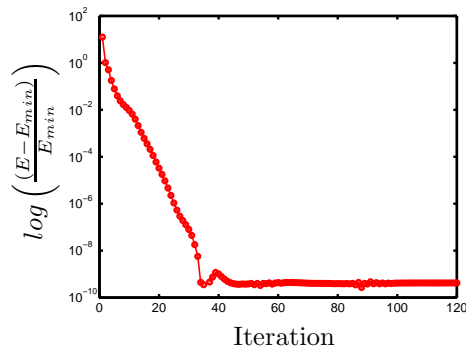


FIG. 5: Energy convergence versus iteration for fcc carbon when the overlap matrix is updated self-consistently, but its variational derivative is not taken into account.

2 Numerical implementation

Specifying the mathematical form of the overlap matrix in one of the forms from the previous section and thus also the forms for \mathbf{C}^Q and H^{eff} leaves the task of evaluating these and related quantities numerically. This section first discusses efficient methods for this evaluation and then describes how to build conjugate gradient minimization from the ability to perform these evaluations.

The term \mathcal{OY}^P must be calculated for defining u , Equation (21), and in the gradient, Equation (22). The

most efficient method for calculating this term is to perform four Fourier transforms per electronic wave function, always multiply terms in the space in which they are diagonal. We find it useful to keep this term in storage so as to only calculate it once in a conjugate gradient loop. Such storage is minimal, as will be seen.

To reduce the time spent in Fourier transforms, we make the approximation of using a slightly smaller Fourier transform grid than might normally be used. The gradient, the \mathbf{C}^Q , and the overlap matrix only involve momentum transfers of $P+Q$. Higher momentum transfers do not occur because H^{QQ} is approximated by H_o^{QQ} , which is diagonal. Accordingly, rather than Fourier grids of size $2Q$, when employ grids of size $P+Q$. We find that using the full Fourier transform grid decreases the energy minimally: for hydrogen and carbon doing so decreases the energy per atom by only $0.5\mu\text{H}$ and $0.8\mu\text{H}$, respectively.

The reduction of the Fourier transform grid to size $P+Q$ from a size of $2Q$, which would be needed in a non-perturbative approach, saves significant storage in the ratio

$$\frac{FFT_{new}}{FFT_{full}} = \frac{1}{8} \left(1 + 3 \left(\frac{E_P}{E_Q} \right)^{\frac{1}{2}} + 3 \left(\frac{E_P}{E_Q} \right) + \left(\frac{E_P}{E_Q} \right)^{\frac{3}{2}} \right). \quad (29)$$

In our boron calculation, this is a factor of nearly three, which can make the difference between being able to perform the calculation on a workstation or requiring parallel computing capability.

We find the following procedure to be very stable for performing conjugate gradient minimization. First, given \mathbf{C}^P generate \mathbf{C}^Q according to Equation (23) or (27). Next, calculate the total energy and the gradient for \mathbf{Y}^P at this point from Equation (22). Holding \mathbf{C}^Q fixed, minimize \mathbf{C}^P along the search direction, and generate a new \mathbf{C}^P , and iterate to convergence.

This procedure for solving for the P -space and generating the Q -space, when needed, is very beneficial for plane-wave calculations when using either the Coulomb potential or a very hard, yet highly transferable, pseudopotentials because, generally for such calculations the computational bottleneck is memory and this approach requires permanent storage only in the P -space. (The Q -space wave functions for a particular band can be generated only when needed.) Moreover, in terms of computational time, a savings of $1 + N_Q/N_P$ for all direct matrix multiplications occurs, and the P -space approach is therefore also more efficient in terms of computational time for systems with many bands.

D Application to the Coulomb Potential

To demonstrate the benefits of our approach, this section presents all-electron calculations for fcc boron at two

different volumes ($V_1 = 3.83 \text{ \AA}^3$ and $V_2 = 3.5 \text{ \AA}^3$), exploring convergence with energy cutoff, usage of memory and computational time, and our ability to predict transferability errors. We carry out all calculations within the local density approximation with ten special k-points in the reduced Brillouin zone and a Fermi surface integration temperature of $kT \approx 0.0037 \text{ H}$.

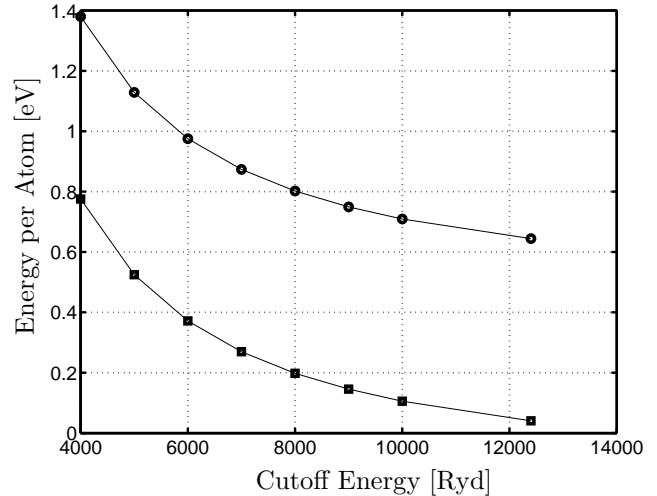


FIG. 6: Energy per atom as a function of cutoff energy for fcc boron, when using the Coulomb potential in the traditional plane-wave approach. The squares correspond $V_1 = 3.83 \text{ \AA}^3$ and the circles correspond to $V_2 = 3.5 \text{ \AA}^3$.

Figure 6 shows the convergence of the energy as a function of cutoff for the direct plane wave approach. The data in the figure demonstrate that the traditional plane-wave approach converges quite slowly, requiring an energy cutoff of over 12000 Ryd to bring the total energy to within 0.1 eV per atom. However, as is well known, the higher-energy plane wave states provide convergence mostly to the inert region of the core near the nucleus and thus physically meaningful energy differences converge much more rapidly than the absolute total energy. As a more meaningful reference, Figure 7 shows the convergence of the energy difference between volume states V_1 and V_2 using the direct plane wave approach.

Figure 8 shows the convergence with P -space cutoff of the total energy when using the perturbative approach with a Q -space cutoff of 7000 Ryd and employing $H_{h,xc}^{cry-at}$ for construction of \mathcal{O} . The figure shows that there is almost no difference in the total energy predictions (circles and squares for the two volume states) when reducing the cutoff in the P -space to 3500 Ryd and that reducing the P -space cutoff down to 1000 Ryd gives just as accurate total energies as a 6000 Ryd cutoff in the traditional approach. The figure also shows that the transferability prediction based on the two core electrons (diamonds) gives the correct order of magnitude and is never off by more than a factor of three in this case.

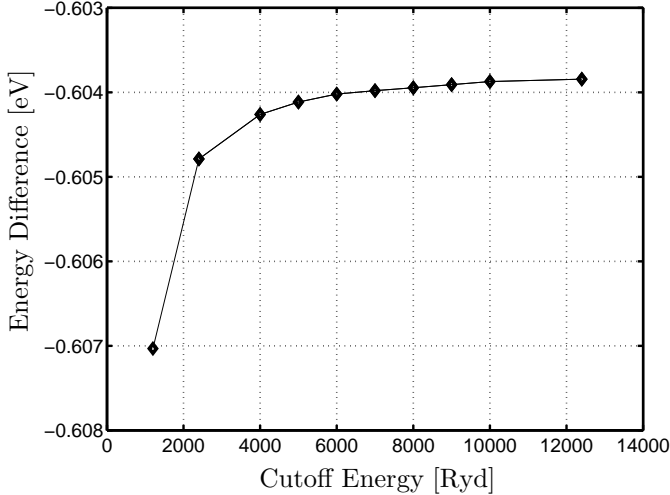


FIG. 7: Energy difference as a function of cutoff for fcc boron, when using the traditional plane-wave approach. The volumes per atom are $V_1 = 3.83 \text{ \AA}^3$ and $V_2 = 3.5 \text{ \AA}^3$.

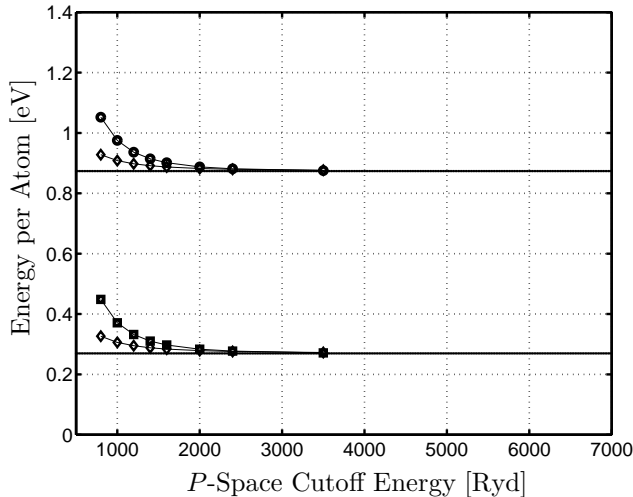


FIG. 8: Energy convergence versus P -space cutoff, using the new method, when $E_c^Q = 7000 \text{ Ryd}$. The squares correspond to $V_1 = 3.83 \text{ \AA}^3$, the circles correspond to $V_2 = 3.5 \text{ \AA}^3$ and the diamonds correspond to the transferability prediction, Equation (19). The horizontal lines correspond to the energy calculated using the traditional approach at a cutoff energy of 7000 Ryd.

Figure 9 shows the performance of the new approach in computing energy differences. Energy differences in the perturbative approach tend to fluctuate slightly and lack the monotonic behavior which the traditional approach exhibits due to loss of ability to describe physical changes in the high momentum states. Perturbation theory recovers these changes nearly perfectly and so the

resulting error in energy difference is smaller and loses systematic behavior. From these results we conclude that a cutoff in the P -space of 1200 Ryd and of 7000 Ryd in the Q -space is more than sufficient to predict accurate energy differences and to capture any unforeseen physical processes which come into play.

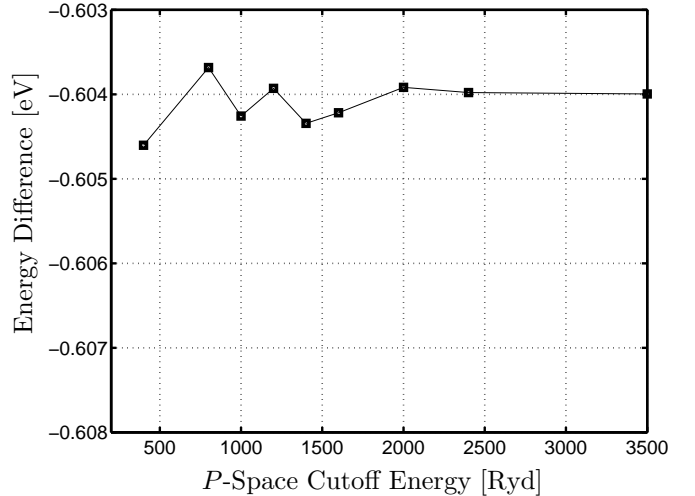


FIG. 9: Energy difference in the new approach as a function of the P -space cutoff.

To make a direct comparison of computational savings, we note that the total energy and energy difference, when using the new method with $E_c^P = 1200 \text{ Ryd}$ and $E_c^Q = 7000 \text{ Ryd}$, is very close to the traditional approach with energy cutoff $E_c^{trad} = 6500 \text{ Ryd}$. At these cutoffs, the memory savings from the perturbative approach is a factor of 12.5 for the wave functions and 2.7 for the FFT's. The time for matrix multiplications decreases by a factor of 5.4 and for Fourier transforms by a factor of 2.7 which largely compensates the need for a few more Fourier transforms in generating \mathbf{C}^Q and $\mathcal{O}Y^P$.

V APPLICATION TO HIGH PRESSURE BORON

As a physical application, we study the high-pressure phases of boron, whose rich physics remains mysterious. Boron is known to exhibit a semiconducting to metallic phase transition at $\approx 170 \text{ GPa}$,² and under high pressure and low temperatures, boron superconducts.² Previous theoretical studies of Boron under pressure include that of Mailhot *et. al.*,⁹ who used both the LMTO method and the pseudopotential method. They have found their pseudopotential results to be more reliable and predict a sequence of structural phase transitions with increasing pressure from the icosahedral structure (α_{12} -B) to a body centered tetragonal structure (bct) to the face-centered

cubic structure (fcc). They find the α_{12} -B \rightarrow bct transition to occur at 210 GPa, and established this as an upper bound for the semiconducting to metallic phase transition.

To calculate the energy for different phases in boron we use our perturbative potential approach with the analytically continued conjugate gradient approach as described in Section IV with \mathcal{O} , \mathbf{C}^Q and H^{eff} calculated as in Section IV D. All calculations employ the local density approximation with the parameterization of Perdew-Zunger³⁷ to the Ceperley-Alder⁴² exchange-correlation energy.

We consider a wider range of structures than explored previously, not only fcc, bct, and α_{12} -B structures but also orthorhombic structures of boron with the α -gallium and β -gallium basis, which we denote as α_{ga} -B and β_{ga} -B, respectively. We consider these orthorhombic structures for a number of reasons. First, Zhu and Henley⁴³ have shown that for 6-coordinated boron under high pressure the triangular lattice is a good candidate for a low energy, high pressure phase, within the density functional theory pseudopotential framework³³ and furthermore such sheets tend to buckle.⁴³⁻⁴⁵ Because the gallium structure can be viewed as stacked sheets of a highly buckled triangular lattice, such a structure is a good candidate for a high pressure phase of boron. Secondly, gallium is another Group III element which has as its ground-state structure α -gallium at low pressures and β -gallium at high pressures,¹⁰ and being under boron in the periodic table supports the notion that such structures are good candidates for a high pressure phase of boron. Below, we show that these structures play quite important roles.

For the bct structure, we use the same $c/a = 0.65$ ratio as was used in Reference,⁹ where this ratio was shown to give the ground state at a volume $\approx 3.91 \text{ \AA}^3$ within the pseudopotential calculation. We have tested this ratio for a number of high pressure states and have found the ideal ratio to remain constant over a wide range of pressures. Hence, we hold c/a at this value for all calculations in our study, and thus our bct energies results represent a quite close upper-bound.

For the α_{12} -B structure, we use the structure listed in Table 5 of Reference,¹⁰ the same used by Mailhiot *et. al.*⁹ This structure is rhombohedral with angle $\alpha = 58.06^\circ$. The basis locations for the atomic positions are

$$\pm(x_1x_1z_1; x_1z_1x_1; z_1x_1x_1; x_2x_2z_2; x_2z_2x_2; z_2x_2x_2),$$

where $x_1 = 0.0104$, $z_1 = -0.3427$, $x_2 = 0.2206$ and $z_2 = -0.3677$. The space group for the α_{12} -B structure is $R\bar{3}m$. Note that we may regard this α_{12} -B structure as representative of the low-pressure states of boron which are all governed by the icosahedron.

For the orthorhombic structures, we use the Gallium structures as found in Wyckoff's book.⁴⁶ For the α_{ga} -B structure, we hold the lattice vector ratios to $a/b = 0.99867$ and $a/c = 0.590035$ and place the atomic ba-

sis at coordinates

$$\pm(0, u, v; 1/2, u+1/2, \bar{v}; 1/2, u, v+1/2; 0, u+1/2, 1/2-v),$$

where $u = 0.0785$ and $v = 0.1525$. The space group is Cmca. For the β_{ga} -B structure, we hold the the lattice vector ratios at $a/b = 0.3567$ and $a/c = 0.9148$ and place the atomic basis at

$$\pm(0, u, 1/4; 1/2, u + 1/2, 1/4),$$

where $u = 0.133$. The space group is Cmcm. Note that we do not optimize the lattice vector ratios for the orthorhombic structures for boron but here hold them fixed to that of gallium at standard conditions. Therefore, the energies which we report for these structures should be regarded simply as upper bounds.

A Convergence

We now establish plane wave cutoffs for our specific study which will both make for practical calculations (particularly for the α_{12} -B structure) and give accurate structural energy differences. For this we shall compare the energy per atom as a function of volume for the fcc, bct and α_{12} -B. As these are convergence tests, we employ relatively modest Brillouin sampling: $4 \times 4 \times 4$, $4 \times 4 \times 6$, and $1 \times 1 \times 1$ (the Γ point) meshes for the fcc, bct and α_{12} -B, respectively. To facilitate integration over the Fermi surface, we employ an electronic temperature of $kT \approx 0.0037 \text{ H}$.

Figure 10 summarizes the results for the three structures when using the plane wave cutoffs from Section IV D, $E_c^Q = 7000 \text{ Ryd}$ and $E_c^P = 1200 \text{ Ryd}$. The curves from the figure are simple fits to

$$E = a_0 + a_1V^{-1/3} + a_2V^{-2/3} + a_3V^{-1}. \quad (30)$$

Having established previously that the above cutoffs give extremely good energy differences, we then searched for possible reductions in the cutoffs which continue to reproduce these results accurately. We find reducing the cutoffs to 200 Ryd for the P -space and 1200 Ryd for the Q -space to both lead to efficient calculations and to give highly accurate results. Figure 11 compares the results at this reduced cutoff (data points) with the previous results at the higher cutoffs (curves).

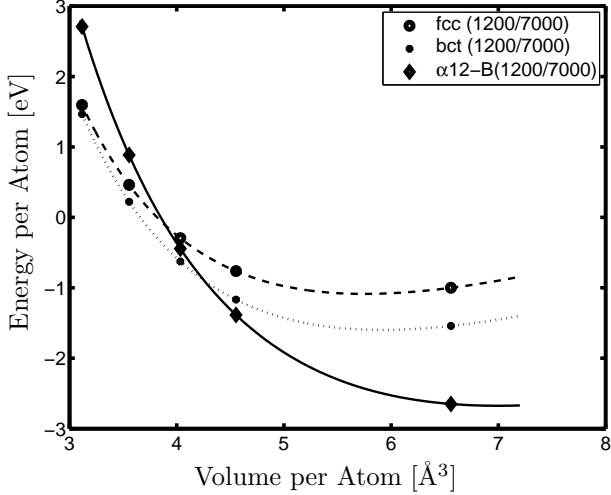


FIG. 10: Energy per atom versus volume per atom for the fcc (circles), bct (stars) and α_{12} -B (diamonds) structures. Energy cutoff for the P -space is 1200 Ryd and for the Q -space 7000 Ryd. The curves are fitted to Equation (30).

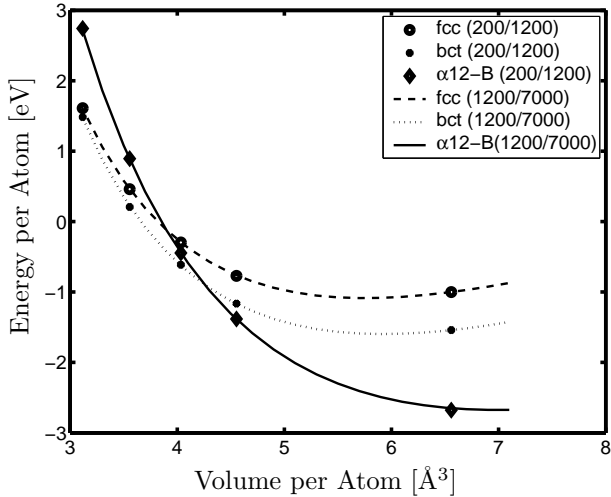


FIG. 11: Energy per atom versus volume per atom. The results from new method using the cutoffs $E_c^P=200$ Ryd and $E_c^Q=1200$ Ryd are displayed as circles (fcc), stars (bct) and diamonds (α_{12} -B). The results from new method using the cutoffs $E_c^P=1200$ Ryd and $E_c^Q=7000$ Ryd are displayed as lines by fitting the data to Equation (30): fcc (dashed), bct (dotted), α_{12} -B (solid).

As a comparison, we also calculate the energy when using a traditional, direct plane-wave approach with a cutoff of 200 Ryd. Figure 12 shows a similar plot, where the points are the plane wave data and the curves represent the fit to the fully converged results. Note that, although fcc structure is fairly well converged at this low

cutoff, there are rather large errors for the α_{12} -B structure. Thus, such a low cutoff is unreliable for the study of such systems. The fact the low cutoff represents one structure well and not another demonstrates the unpredictability of transferability errors, underscores the need to predict those errors reliably, and places pseudopotential studies of such systems, which assume that errors in processes at such high energy scales cancel, in doubt.

Finally, we note that the memory savings of using the new method, with cutoffs of 200 Ryd and 1200 Ryd, versus the traditional approach, which would require a cutoff of 1200 Ryd to produce results of similar reliability, is quite substantial, a factor of ≈ 15 for wave functions and ≈ 3 for the FFT box. The time for the matrix multiplication correspondingly reduces by a factor of 6 and for the Fourier transforms by a factor of 3, similar to Section IV D. Because of these savings, particularly in memory, all of our calculations below were possible on a single desktop computer and there was no need for parallel supercomputing.

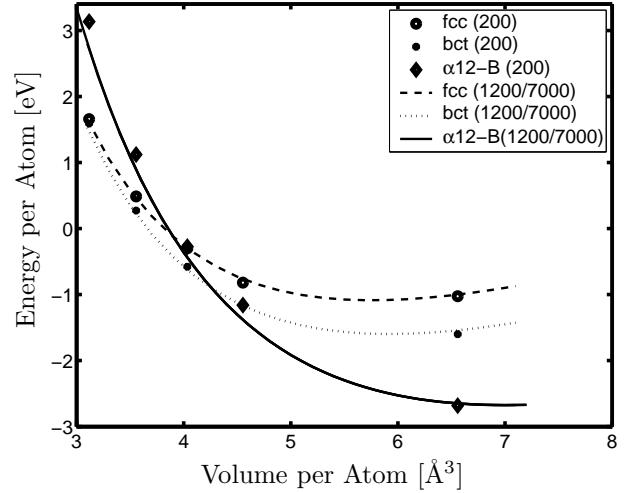


FIG. 12: Energy per atom versus volume per atom. The results from using the traditional approach with cutoff $E=200$ Ryd are displayed as circles (fcc), stars (bct) and diamonds (α_{12} -B). The results from new method using the cutoffs $E_c^P=1200$ Ryd and $E_c^Q=7000$ Ryd are displayed as lines by fitting the data to Equation (30): fcc (dashed), bct (dotted), α_{12} -B (solid).

B Results

Having found appropriate plane wave cutoffs, we next converged both the Brillouin sampling and the fictitious Fermi temperature. We find that a fictitious Fermi temperature of $kT = 0.001H$ converges the total energy to a within a few tenths of a millihartree per atom ($0.2mH$ for

the fcc structure). For the fcc and bct structures, Brillouin sampling on $6\times 6\times 6$ and $4\times 4\times 6$ meshes, respectively, suffice to converge the total energy per atom to within the same tolerance. We then generate meshes for the remaining structures by maintaining the same reciprocal space sampling density as closely as possible, resulting in meshes of size $2\times 2\times 2$, $4\times 4\times 4$ and $6\times 4\times 6$ for the α_{12} -B, α_{ga} -B and β_{ga} -B structures, respectively.

Figure 13 shows our final results, which are converged to within a few tenth of a millihartree per atom. Most notably, we find a new phase, the α_{ga} -B, to be the lowest in energy phase under high pressure. α_{ga} -B boron becomes energetically favorable over α_{12} -B boron at a pressure of 71 GPa, and remains the energetically favored phase up to the highest pressures we have studied, which are over 500 GPa. Although there are other structures in the same icosahedral family for boron, due to the dramatic rise in energy of the α_{12} -B structure, we do not expect these alternate structures to have a significantly lower energies. Finally, optimizing the lattice vectors ratios for the orthorhombic phases will only make them more favorable. We, therefore, expect our prediction of a phase transition from the icosahedral family to the α_{ga} -B structure to be robust.

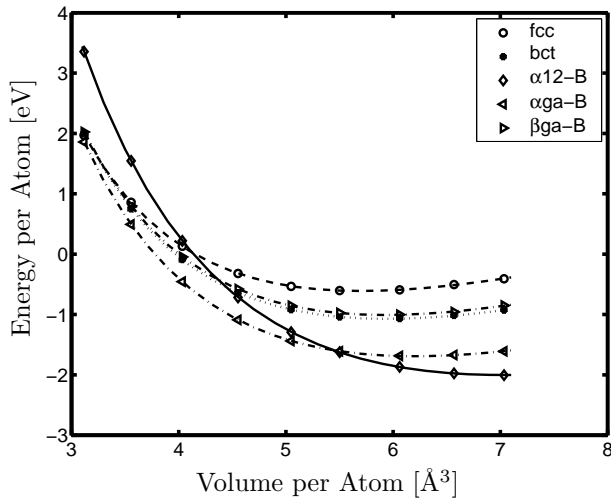


FIG. 13: Energy per atom versus volume per atom, for the fcc (circles), bct (stars), α_{12} -B (diamond), α_{ga} -B (left facing triangles) and β_{ga} -B (right facing triangles) structures. The results are from the new method using the cutoffs $E_c^P=200$ Ryd and $E_c^Q=1200$ Ryd.

As a point of comparison to the existing pseudopotential calculations,⁹ which had not considered the orthorhombic structures, ignoring those structures, we also find the sequence of transitions α_{12} -B \rightarrow bct \rightarrow fcc. Although our value of 194 GPa for the first of these transitions agrees well with the pseudopotential result of 210 GPa, our prediction of ≈ 475 GPa for the second transition differs substantial from the pseudopotential result

of 360 GPa. This large discrepancy most likely results from the inadequacies of the pseudopotential to effectively account for the response within the core. The inconsistent performance of the pseudopotential results underscores the importance of control over transferability when studying high pressure systems.

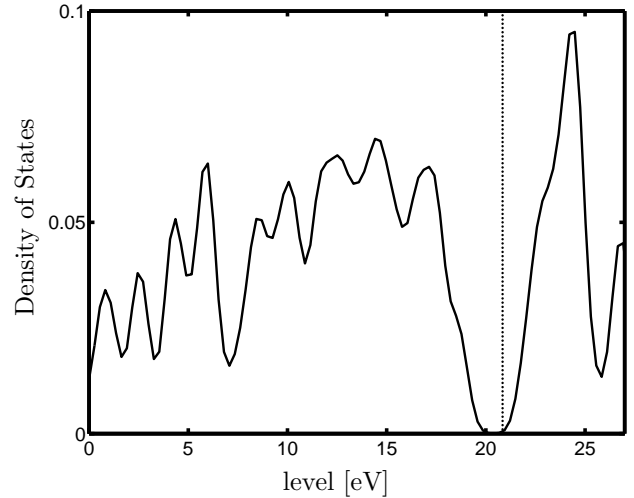


FIG. 14: Density of states for the valence electrons for the α_{ga} -B structure. The straight line corresponds to the chemical potential at $kT = 0.001H$.

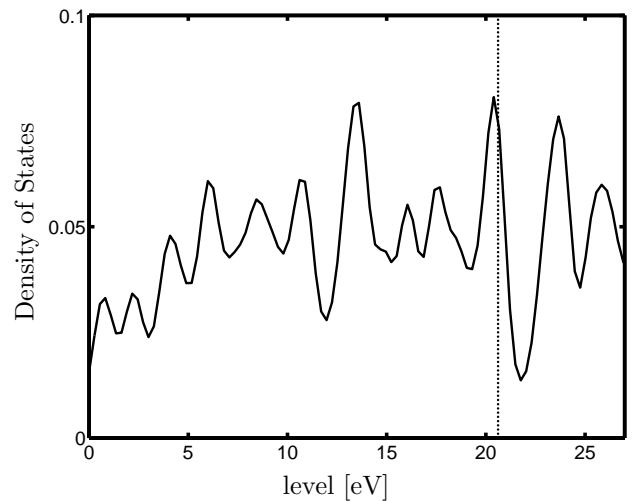


FIG. 15: Density of states for the valence electrons for the β_{ga} -B structure. The straight line corresponds to the chemical potential at $kT = 0.001H$.

Given the availability of high-pressure resistivity data for boron,² it is interesting to consider the electronic structure of the hitherto unexplored α_{ga} -B phases for boron. Figures 14 and 15 show low-resolution plots of the

density of states for α_{ga} -B and β_{ga} -B boron at 250 GPa and 217 GPa, respectively, as generated using the Brillouin zone sampling from the total energy calculations. The plots have low resolution because, as is well known, meshes which give reliable total energies often are too modest to give detailed density of states. (Providing smooth curves required a Gaussian broadening of width 1 eV.) The figures clearly show that, whereas the β_{ga} -B phase is semimetallic, the density of states of the α_{ga} -B phase clearly exhibits a gap at the Fermi level, even at high pressures.

Experimentally, the room-temperature resistance of boron decreases discontinuously as a function of pressure at 30 GPa, 110 GPa and 170 GPa.² In comparing our results to these data, it is important to recall that the α_{12} -B structure is only meant to be representative of the icosahedral family of low-pressure structures and that, with optimization of the aspect ratios, the curves for the α_{ga} -B and β_{ga} -B structures will displace to even lower energies. In particular, a downward shift of only 0.15 eV (10%) in the α_{ga} -B curve would lower our prediction for the α_{12} -B $\rightarrow\alpha_{ga}$ -B transition from 71 GPa to 30 GPa. Thus, while further investigation is clearly needed, these data suggest that a structural transition from the icosahedral family to the orthorhombic phase is a viable candidate for the resistance discontinuity observed in boron at 30 GPa.

Because Boron is observed experimentally to be metallic above 160 GPa, our results imply that another, yet unexplored, structure must become energetically favored at this pressure and be responsible for the highest of the observed discontinuities in the room-temperature resistance. Whatever this metallic structure is, it cannot be simple as the fcc, bct, bcc and hcp structures because none are competitive at high pressures. It is suggestive, however, that our energetic upper-bound for the metallic β_{ga} -B structure is quite competitive with the fcc and bct structures at the very highest pressures. Although further calculations would certainly be needed to verify this conjecture, it is quite possible that the observed discontinuity in the resistivity at 170 GPa represents a structural transition from the semiconducting α_{ga} -B to the metallic β_{ga} -B phase.

VI CONCLUSIONS

We have developed a new method which allows for dramatic reduction in the number of plane waves needed in all-electron density functional theory calculations or in calculations with hard, but highly transferable pseudopotentials. The foundation of the approach is to treat the higher energy plane wave components of the electronic states implicitly through a perturbative approach, thereby allowing these components to be recovered quickly only when needed, thus alleviating memory storage requirements by factors as high as fifteen in

practical calculations. The approach lends itself well to current optimized minimization techniques such as conjugate gradient methods and has the benefit of allowing quantitative estimates of transferability to new systems for which there is little or no experience and for which the transferability of pseudopotentials is in question, such as condensed matter at high pressure where effects in the core region become much more important.

In addition, the first application of this approach has led to new intriguing conjectures as to the structure of boron at high pressures. We have carried out the first *ab initio* calculations of the orthorhombic structures of boron, which we show to play an important role in the high pressure behavior of this material. We find that, prior to becoming metallic, boron makes a phase transition from the icosahedral family to the semiconducting α_{ga} -B structure. The low energy of this semiconducting phase indicates that the structure of the superconducting phase for boron is more complicated than the simple monotonic lattices explored to date. While further calculations including optimization of the lattice ratios for the orthorhombic phases are needed, our results lead to the conjecture that the metallic β_{ga} -B structure is a good candidate for the superconducting phase.

VII ACKNOWLEDGMENTS

D.E.S. would like to thank Chris Henley for suggesting the orthorhombic structures and useful discussions, Bill Goddard for his generous hospitality during his stay at Cal-Tech, Peter Lepage for initiating our interest in this work and Matt Evans for useful discussions. D.E.S. also thanks T.A.A. for support through the MIT Department of Physics.

A APPLICATION TO KLEINMAN-BYLANDER PSEUDOPOTENTIALS

This appendix reviews briefly the application of our approach to norm-conserving pseudopotentials of the Kleinman-Bylander form, where the approach essentially becomes a softening procedure without transferability biases. The softening comes at the cost of generating a generalized eigenvalue problem, similar in spirit to the ultrasoft pseudopotential (USSP)⁴⁰ and projector augmented wave (PAW)²⁶ methods. However, unlike the USSP and PAW approaches, where the softening takes place referenced to a spherical atomic environment, in our approach the softening occurs in the full crystalline environment and thereby includes nonlocal interactions from multiple scattering events from different atoms in the crystal but at minimal extra computational cost.

Here, we develop the approach to work with standard separable non-local potentials of the form

$$H_{nl}(\vec{G}, \vec{G}') = \sum_{at, pr} |V_{at, pr}(\vec{G})\rangle f_{pr} \langle V_{at, pr}(\vec{G}')|, \quad (1)$$

where the sum is over all atoms in the cell and all projectors on a given atom. For such potentials it proves much more computationally efficient to use the forms similar to Equations (26), (27) and (28) for the overlap matrix \mathcal{O} , \mathbf{C}^Q and H^{eff} , respectively. The overlap matrix then takes the form

$$\mathcal{O} = 1 + \left(H_{nl}^{PQ} + H_{loc}^{cr-at, PQ} \right) \frac{1}{H_o^{QQ} H_o^{QQ}} \left(H_{nl}^{QP} + H_{loc}^{cr-at, QP} \right)$$

where H_{loc}^{cr-at} is the local term for the “free-atom” crystal, a crystal whose charge density is a direct superposition of the charge densities from isolated atoms. This term includes the local part of the ionic potential, the Hartree term and the exchange-correlation term. Ignoring the identity, expansion of Equation (2) results in four terms, which we refer to as nonlocal-nonlocal, nonlocal-local, local-nonlocal and local-local, respectively. The local-local term is exactly the same as that of the Coulomb potential and therefore should be treated as in the manuscript. The advantage of employing a fixed, rather than self-consistent, overlap matrix is that each of the remaining terms contract onto the P -space only. We now consider each of these in turn.

The \vec{p}, \vec{p}' component of the nonlocal-nonlocal term is

$$\mathcal{O}_{nl, nl}(\vec{p}, \vec{p}') = \sum_{\substack{at, pr \\ at', pr'}} |V_{at, pr}(\vec{p})\rangle f_{pr} A_{at, pr}^{(2)} f_{pr'} \langle V_{at', pr'}(\vec{p}')|, \quad (3)$$

where

$$A_{at, pr}^{(2)} = \sum_{\vec{q}} \langle V_{at, pr}(\vec{q}) | \left(\frac{1}{\frac{1}{2}\vec{q}^2} \right)^2 | V_{at', pr'}(\vec{q}) \rangle. \quad (4)$$

This term quantifies how the high-momentum states couple to the ions, including not only couplings to individual atoms but also to pairs of atoms through $A_{at, pr}^{(2)}$, thereby including environmental effects directly into the potential and enhancing transferability. In terms of implementation, this term requires almost no additional memory as the only additional storage is for $A^{(2)}$ and scales as $N_b \times N_b$, where N_b is the number of bands. The computational demands are quite light as $A^{(2)}$ requires an amount of computing comparable to a single orthonormalization of the electronic bands and only need be compute once at the very beginning of the calculation.

The local-nonlocal and nonlocal-local terms are just hermitian conjugates of each other. The \vec{p}, \vec{p}' component

of the nonlocal-local term has the form

$$\mathcal{O}_{nl, loc}(\vec{p}, \vec{p}') = \sum_{at, pr} |V_{at, pr}(\vec{p})\rangle f_{pr} \langle F_{at, pr}^{(2)}(\vec{p}')|, \quad (5)$$

where

$$\langle F_{at, pr}^{(2)}(\vec{p}')| = \langle V_{at, pr}(\vec{q}) | \left(\frac{1}{\frac{1}{2}\vec{q}^2} \right)^2 H_{loc}^{cr-at}(\vec{q} - \vec{p}'). \quad (6)$$

$F^{(2)}$ can also be simply calculated in the beginning of the calculation through Fourier transforms of $(2) \langle V_{at, pr}(\vec{q}) | \left(\frac{1}{\frac{1}{2}\vec{q}^2} \right)^2 |$.

The effective Hamiltonian H^{eff} can also be contracted onto the P -space. H^{eff} has the form

$$H^{eff} = - \left(H_{loc}^{PQ} + H_{nl}^{PQ} \right) \frac{1}{H_o^{QQ}} \left(H_{loc}^{cr-at, QP} + H_{nl}^{cr-at, QP} \right).$$

The nonlocal term on the left-hand side can be contracted onto $H_{loc}^{cr-at, QP}$ in a similar fashion as was done to \mathcal{O} , giving two terms:

$$H_{nl, nl}(\vec{p}, \vec{p}') = \sum_{\substack{at, pr \\ at', pr'}} |V_{at, pr}(\vec{p})\rangle f_{pr} A_{at, pr}^{(1)} f_{pr'} \langle V_{at', pr'}(\vec{p}')|, \quad (7)$$

where

$$A_{at, pr}^{(1)} = \sum_{\vec{q}} \langle V_{at, pr}(\vec{q}) | \left(\frac{1}{\frac{1}{2}\vec{q}^2} \right) | V_{at', pr'}(\vec{q}) \rangle, \quad (8)$$

and

$$H_{nl, loc}(\vec{p}, \vec{p}') = \sum_{at, pr} |V_{at, pr}(\vec{p})\rangle f_{pr} \langle F_{at, pr}^{(1)}(\vec{p}')|, \quad (9)$$

where

$$\langle F_{at, pr}^{(1)}(\vec{p}')| = \langle V_{at, pr}(\vec{q}) | \left(\frac{1}{\frac{1}{2}\vec{q}^2} \right) H_{loc}^{cr-at}(\vec{q} - \vec{p}'). \quad (10)$$

This will reduce almost all matrix multiplications onto the P -space. The only remaining Q -space multiplication would be in $H_{loc, nl}$. A final simplification that can be made is to take

$$H^{eff} = -H^{cr-at, PQ} \frac{1}{H_o^{QQ}} H^{cr-at, QP},$$

and thereby make the full effective Hamiltonian contractible onto the P -space.

REFERENCES

- ¹ For a recent review see: *Rev. High Pressure Sci. Technol.*, 7, 1998.

- ² M.I. Eremets, V.V. Struzhkin, H.-k. Mao, and R.J. Hemley. *Science*, 293:272, 2001.
- ³ J.B. Neaton and N.W. Ashcroft. *Nature*, 400:141, 1999.
- ⁴ J.B. Neaton and N.W. Ashcroft. *Phys. Rev. Lett.*, 86:2830, 2001.
- ⁵ V.V. Struzhkin, R.J. Hemley, and H.K. Mao. *Bull. Am. Phys. Soc.*, 44:1489, 1999.
- ⁶ F.E. Fortov, et. al. *JETP Lett.*, 70:628, 1999.
- ⁷ M. Hanfland, K. Syassen, N.E. Christensen, and D.L. Novikov. *Nature*, 408:174, 2000.
- ⁸ Y.K. Vohra, K.E. Brister, S. Desgreniers, A. Ruoff, K.J. Chang, and M.L. Cohen. *Phys. Rev. Lett.*, 56:1944, 1986.
- ⁹ C. Mailhot, J.B. Grant, and A.K. McMahan. *Phys. Rev. B*, 42:9033, 1990.
- ¹⁰ J. Donohue. *The Structures of the Elements*, page 48. Wiley, New York, 1974.
- ¹¹ In D. Emin, T. Aselage, C.L. Beckel, I.A. Howard, and C. Wood, editors, *Boron-Rich Solids, AIP Conference Proceedings 140*, Albuquerque, New Mexico, 1986. American Institute of Physics.
- ¹² Ihm, J., A. Zunger, and M.L. Cohen. *J. Phys. C*, 12:4409, 1979.
- ¹³ B.G. Johnson, P.M.W. Gill, and J.A. Pople. *J. Chem. Phys.*, 98:5612, 1993.
- ¹⁴ D.J. Singh. *Planewaves, Pseudopotentials and the LAPW Method*. Kluwer Academic, Norwell, MA., 1994.
- ¹⁵ In H. Dreysse, editor, *Electronic Structure and Physical Properties of Solids, The Uses of the LMTO Method*, Lectures of a Workshop Held at Mont Saint Odile, France, October 2-5, 1998, 2000. Springer-Verlag.
- ¹⁶ T.A. Arias. *Rev. Mod. Phys.*, 71:267, 1999.
- ¹⁷ T.W. Barbee III and M.L. Cohen. *Phys. Rev. B*, 44:11563, 1991.
- ¹⁸ V. Natoli, R.M. Martin, and D.M. Ceperley. *Phys. Rev. Lett.*, 70:1952, 1993.
- ¹⁹ L. Bellaiche and K. Kunc. *Phys. Rev. B*, 55:5006, 1997.
- ²⁰ D.R. Hamann, M. Schluter, and C. Chiang. *Phys. Rev. Lett.*, 43:1494, 1979.
- ²¹ L. Kleinman and D.M. Bylander. *Phys. Rev. Lett.*, 48:1425, 1982.
- ²² W. Pickett. *Comput. Phys. Rep.*, 9:115, 1989.
- ²³ M. Teter. *Phys. Rev. B*, 48:5031, 1993.
- ²⁴ I. Grinberg, N.J. Ramer, and A.M. Rappe. *Phys. Rev. B*, 63:201102, 2001.
- ²⁵ S.G. Louie, S. Froyen, and M.L. Cohen. *Phys. Rev. B*, 26:1738, 1982.
- ²⁶ P.E. Blochl. *Phys. Rev. B*, 50:17953, 1994.
- ²⁷ P.-O. Lowdin. *J. Chem. Phys.*, 19:1396, 1951.
- ²⁸ H. Feshbach. *Ann. Phys. N.Y.*, 19:287, 1962.
- ²⁹ I. Lindgren and J. Morrison. *Atomic Many-Body Theory*. Springer-Verlag, Berlin, 1982.
- ³⁰ D. Vanderbilt and J.D. Joannopoulos. *Phys. Rev. B*, 27:6296, 1983.
- ³¹ M.T. Yin and M.L. Cohen. *Phys. Rev. B*, 26:3259, 1982.
- ³² R. Car and M. Parrinello. *Phys. Rev. Lett.*, 55:2471, 1985.
- ³³ M.C. Payne, M.P. Teter, D.C. Allen, T.A. Arias, and J.D. Joannopoulos. *Rev. Mod. Phys.*, 64:1045, 1992.
- ³⁴ M.P. Teter, M.C. Payne, and D.C. Allan. *Phys. Rev. B*, 40:12255, 1989.
- ³⁵ T.A. Arias, M.C. Payne, and J.D. Joannopoulos. *Phys. Rev. Lett.*, 69:1077, 1992.
- ³⁶ S. Ismail-Beigi and T.A. Arias. *Comput. Phys. Comm.*, 128:1, 2000.
- ³⁷ J.P. Perdew and A. Zunger. *Phys. Rev. B*, 23:5048, 1981.
- ³⁸ S. Goedecker, M. Teter, and J. Hutter. *Phys. Rev. B*, 54:1703, 1996.
- ³⁹ H.J. Monkhorst and J.D. Pack. *Phys. Rev. B*, 13:5188, 1976.
- ⁴⁰ D. Vanderbilt. *Phys. Rev. B*, 41:7892, 1990.
- ⁴¹ M. Frigo and S.G. Johnson. Fftw: An adaptive software architecture for the fft. In *ICASSP conference proceedings*, page 1381, 3.
- ⁴² D.M. Ceperley and B.J. Alder. *Phys. Rev. Lett.*, 45:566, 1980.
- ⁴³ W.-J. Zhu and C.L. Henley *Europhys. Lett.*, 51:133, 2000.
- ⁴⁴ I. Boustani and A. Quandt and P. Kramer *Europhys. Lett.*, 36:583, 1996.
- ⁴⁵ I. Boustani and A. Quandt *Europhys. Lett.*, 39:537, 1997.
- ⁴⁶ R.W.G. Wyckoff. *Crystal Structures*, page 22-23. 2nd ed., vol I. Interscience Publishers, New York, c1963